Supplementary Materials

1. Materials and Methods

Materials: $Sr_3Ir_2O_7$ single crystals were synthesized using the self-flux flux method as described in Reference [1] and references therein.

Ultrafast Transient Reflectivity measurements: (Figure 2, main text) were performed using a Legend Elite amplifier (Coherent) with 800 nm central wavelength, 40 nm bandwidth a pulse duration of ~35 fs with and an energy of 5 W at 5 kHz repetition rate. The broadband visible probe light was generated by focusing a small fraction of the 800 nm beam onto a sapphire crystal while 800 nm light was mechanically chopped at 2.5 kHz and was used as the pump pulse. The pump energy was adjusted using a half wave plate on a motorized stage capable of rotating the polarization of the beam relative to a Brewster polarizer. Both beams were focused on the sample and to ensure probing of a homogeneously pumped region, the probe size ($\sim 4 \cdot 10^{-5}$ cm^2) was made smaller than the pump size ($\sim 2 \cdot 10^{-4}$ cm^2). The changes in the reflectivity of the sample were detected using a commercial Andor Zyla sCMOS camera. The cryogenic measurements were performed using liquid nitrogen cryostat (Oxford Instruments, Optistat DN-V).

Static Reflectivity measurements (Figure 1A, main text) were performed on the same sample used in the pump-probe measurements in the cryostat that was also used for the transient reflectivity measurements. A thermal Tungsten-Halogen lamp (Thorlabs SLS201L) was coupled to a multimode fibre and the output imaged onto the sample using a 4f configuration, with a sub-millimeter spot size and an angle of incidence of a few degrees. The reflected light was collected using a second 4f-lens configuration onto a multimode fibre. A cosine corrector was used to reduce the effect of sample drift on the coupling efficiency, and a camera was used to log the sample position in real time to monitor thermal drift. The final spectrum was collected using a silicon CCD spectrometer with 5s exposures (Avantes AvaSpec-Mini4096CL-UVI10). For clarity Figure 1A (main text) displays the measured reflectivity relative to the value at 77 K.

2. Analysis of coherent phonons

The transient reflectivity data shown in Figure 2 (main text) is highly modulated at all probe wavelengths by large amplitude oscillations associated with coherent phonons generated by the pump excitation. To extract the frequency of the oscillations the transient data was first differentiated in order to remove the incoherent exponential decay component. Subsequently a fast Fourier transform (FFT) of the resulting differential map yielded a 2D plot of frequency vs probe wavelength. To avoid any coherent artefact at $t \sim 0$ ps, the dataset was analysed only between 0.3 – 5.5 ps. To obtain a higher signal to noise level, the frequency map was average at all wavelength yielded modes at ~146 cm^{-1} and ~182 cm^{-1} (Figure 4A, main text). The values obtained are in good agreement with those measured with equilibrium Raman spectroscopy [2] and previous ultrafast optical spectroscopy measurements [3]. In order to obtain the frequency value at each fluence (Figure 4B, main text), the differential map at each wavelength was first fitted by the sum of two Gaussians giving by the expression

$$f(x) = A_1 e^{-\left(\frac{x-x_{01}}{w_1}\right)^2} + A_2 e^{-\left(\frac{x-x_{02}}{w_2}\right)^2}$$

Where Ai, x_{0i}, and w_i (i=1,2) are the amplitude, central frequency and width of the modes. Subsequently, we calculate the average value of the central frequency (x_{0i}) of each Gaussian in the probe wavelength range which yields the frequency value shown in Figure 4B (main text). The error bars correspond to the standard deviation of the average calculation for each fluence. Figure S9 shows the different steps of this analysis performed at 77 K and 295 K.

An alternative way to verify such strong fluence dependence of the ~146 cm^{-1} mode at 77 K is by directly fitting the differentiated transient data at different fluence focusing on the 650-700 nm region where this mode shows its maximum intensity and the ~182 cm^{-1} mode contribute less. The differentiated transient data was fit with the equation

$$f(t) = Acos\left(\frac{2\pi f_1}{T_1} + \varphi_1\right)e^{-t/\tau_1} + Bcos\left(\frac{2\pi f_2}{T_2} + \varphi_2\right)e^{-t/\tau_2}$$

where A, f_1, T_1, φ_1 and τ_1 correspond to the amplitude, frequency, period, phase and constant time of the low energy mode respectively. Analogously, the second term of the equation correspond to the high energy mode.

Figure S7 A shows the perfect match between the raw data (circles) and the fit (solid lines) at different fluence values at 77 K. Figure S7 B shows the amplitude parameter from the fit. It shows a similar behaviour on both modes with fluence as observed in Figure 4D (main text).

3. Calculation of the magnetic contribution

The transient reflectivity at different delay times (t), probe wavelengths (λ) and fluences (F) shows changes at T_N as $\Delta R=\Delta R(T, \lambda, t, F)=\Delta R_e+\Delta R_M$ where ΔR_M and ΔR_e are the magnetic and non-magnetic (e.g. electronic) contributions respectively. A such, $\Delta R_M=0$ for $T>T_N$. Therefore, ΔR_M can be obtained provided that ΔR_e is known. Ideally, the transient response of the electronic system would be a separable function of the different variables (T, λ, t, F), i.e. $\Delta R_e=f(T)g(\lambda)h(t)k(F)$ allowing the functions $g(\lambda)h(t)k(F)$ to be obtained from the high temperature data ($>T_N$). In such case the behaviour of the electron system, f(T), could be obtained below T_N. However, we were unable to reliably separate the dataset into functions of specific variables, and no unique spectral function for the electronic degrees of freedom could be found. Therefore, we bypassed this issue by identifying those wavelengths (λ_{e0}) at which $(d\Delta R_e)/dT(\lambda_{e0})=0$. We found that that the region around $\lambda_{e0}\approx600$ nm fulfilled this condition. Note that ΔR_e is not zero, nor is it a constant as a function of time (Figure S3). We assume that the above criteria remains true at this wavelength below T_N and obtain the magnetic contribution as $\Delta R_M= \Delta R(T<T_N,\lambda_{e0},t, F)-\Delta R(T> T_N,\lambda_{e0},t, F)$ as shown in Figure S4 and Figure 3 (main text). The validity of this approach is further corroborated by comparison of the optically extracted ΔR_M with the magnetic Bragg peak obtained from reference [4].

4. Comparison of XFEL and Optical data

The X-ray data used in Figure 3D (main text) and reported in reference [4] was performed under grazing incidence and with a 2 μm pump wavelength, whereas the optical work presented herein is performed at 800 nm and a 45 degree angle of incidence. Differences in absorption and reflection

coefficients as well as penetration depth miss-matches prevents directly comparing the amplitude of the change and fluence values. In addition, the base temperature of the XFEL data is known with less precision due to the use of a cryo-stream cooling system as opposed to the liquid nitrogen cryostat employed in the optical measurements that allows for fine, controlled changes in temperature. Furthermore, the Magnetic Bragg peak data saturates at a value of ~70% due to the pump probe miss-match between laser and X-rays. This difference should be much smaller at visible wavelengths. Therefore, to correct for this, we scale the magnitude of the X-ray data by a constant factor.

5. Details of the Monte Carlo Calculations

Monte Carlo (MC) algorithms and models are commonly used to study equilibrium processes in a variety of systems in physics and beyond. However, they can also be applied to the investigation of dynamical processes [5,6]. Although it is common to implement more complex models [7], in this work we opt for the simplest possible description of an antiferromagnet: the 3D spin-1/2 Ising model with nearest neighbours interaction. We find that this model, in its simplicity, is capable of capturing the essence of the magnetization dynamics after photoexcitation and to qualitatively reproduce the experimental observations.

We model the generation of doubly occupied spin states upon laser excitation as direct spin flips. The modeled system consisted of a 3D simple cubic lattice of lateral size L=100 spins (N=1000000 spins in total). A MC step (MCS) is defined as N attempted spin flips for a system of size N. The system was prepared in a perfectly aligned low temperature state and suddenly disordered at time t=2 MCS by flipping a given percentage of the spins (a percentage calculated from the desired demagnetization value) following a random distribution. After that, the system was let free to evolve for a given number of MC steps. The equilibration was implemented using a Metropolis-Hastings algorithm with Glauber dynamics. At each step the staggered magnetization was measured as the difference of the magnetizations of the two sublattices, which were measured as the sum of all the spins alignment in the sublattice.

In the Monte Carlo dynamics, energy is not conserved. Optical excitation, through spin-flips, increases the energy in the system, but as the magnetic order recovers, the total energy of the system decreases. In a real system this energy would translate to an increase in the temperature. As the probability for spin flips increases with increasing Monte Carlo temperature, it may be expected that such a temperature rise may result in more rapid dynamics as the system can more easily leave local minima. Therefore, a second simulation was performed including an increase in temperature together with the demagnetization. The amplitude of the increase in temperature is proportional to the change in the magnetization. The temperature profile is described by:

$$T = T_O + M \cdot C \cdot (1 - e^{-\frac{t}{\tau}})$$

Where $T_0 = 0.33T_N$ is the initial temperature, M is the change in magnetization, $C/T_N = 0.56$ is a proportionality constant, which defines the maximum temperature rise relative to a given demagnetization and can be thought of as a heat capacity which converts the non-thermal demagnetization into a temperature. The choice of C=0.56 ensures that the temperature increases substantially above the initial temperature while remaining lower that the transition temperature. This corresponds to a final temperature of 0.89 T_N which is just below the value at which the phase transition starts to affect the dynamics. t is the time in MCS and τ is the characteristic time of the increase in temperature. τ is set to be 1MCS to roughly match the fast time constant in the low

fluence simulation. However, the resulting dynamics did not change if the temperature rise was considered to be a step function in time. The top panel of Figure S8 reports the result of such simulation along with the corresponding temperature profile in the bottom panel. The presence of the temperature change does not affect the magnetization dynamics which looks very similar to those reported in Figure 5 in the main text as long as the lattice temperature remained below T_N.

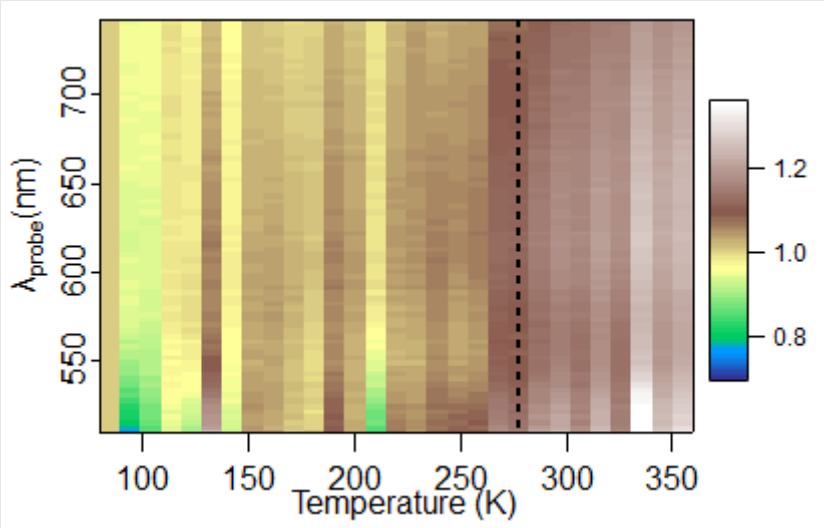

Figure S1: Raw temperature dependence of the static reflectivity which was smoothed in Figure 1A of the main text. The signal is shown relative to the value at 77 K (AFM).

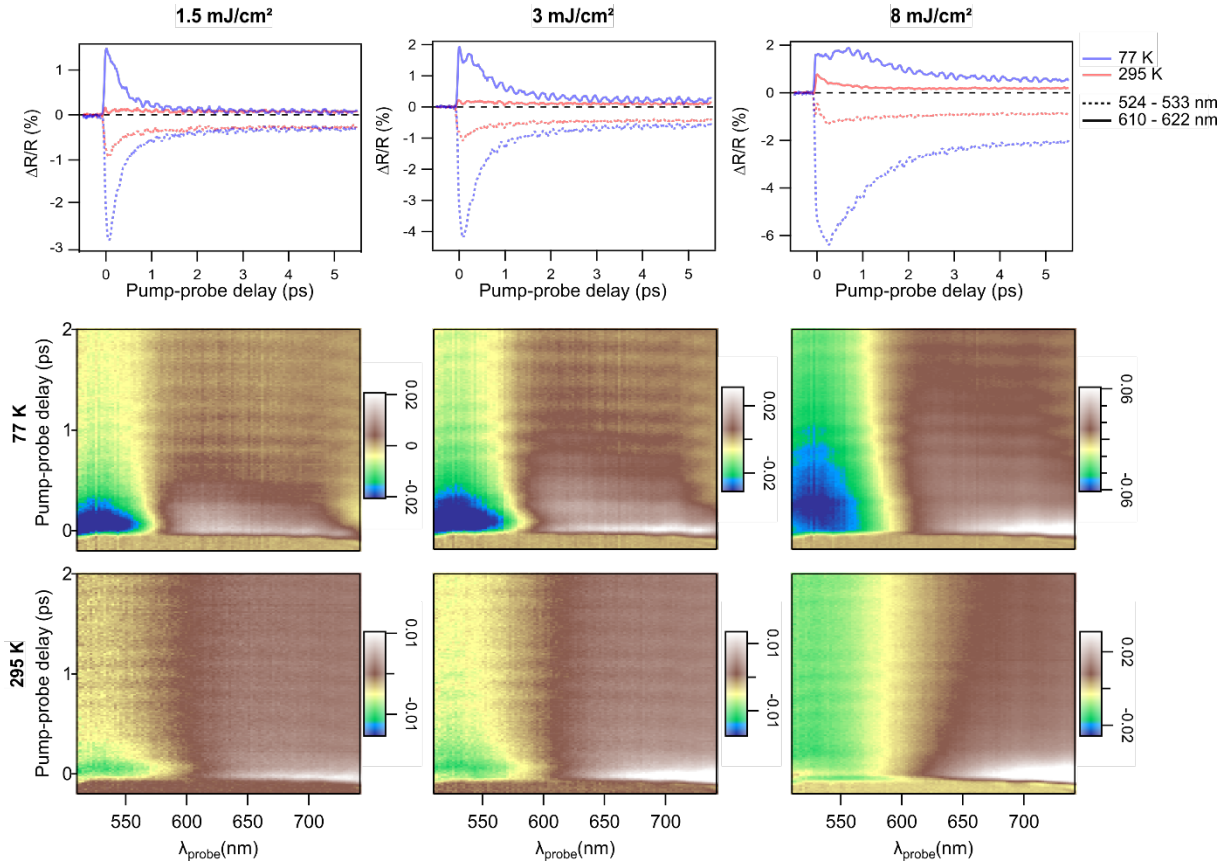

Figure S2: Transient Reflectivity change upon 800nm excitation at 77 K (top) and 295 K (bottom) measured at F = 1.5 mJ cm^{-2}, 3 mJ cm^{-2} and 8 mJ cm^{-2}.

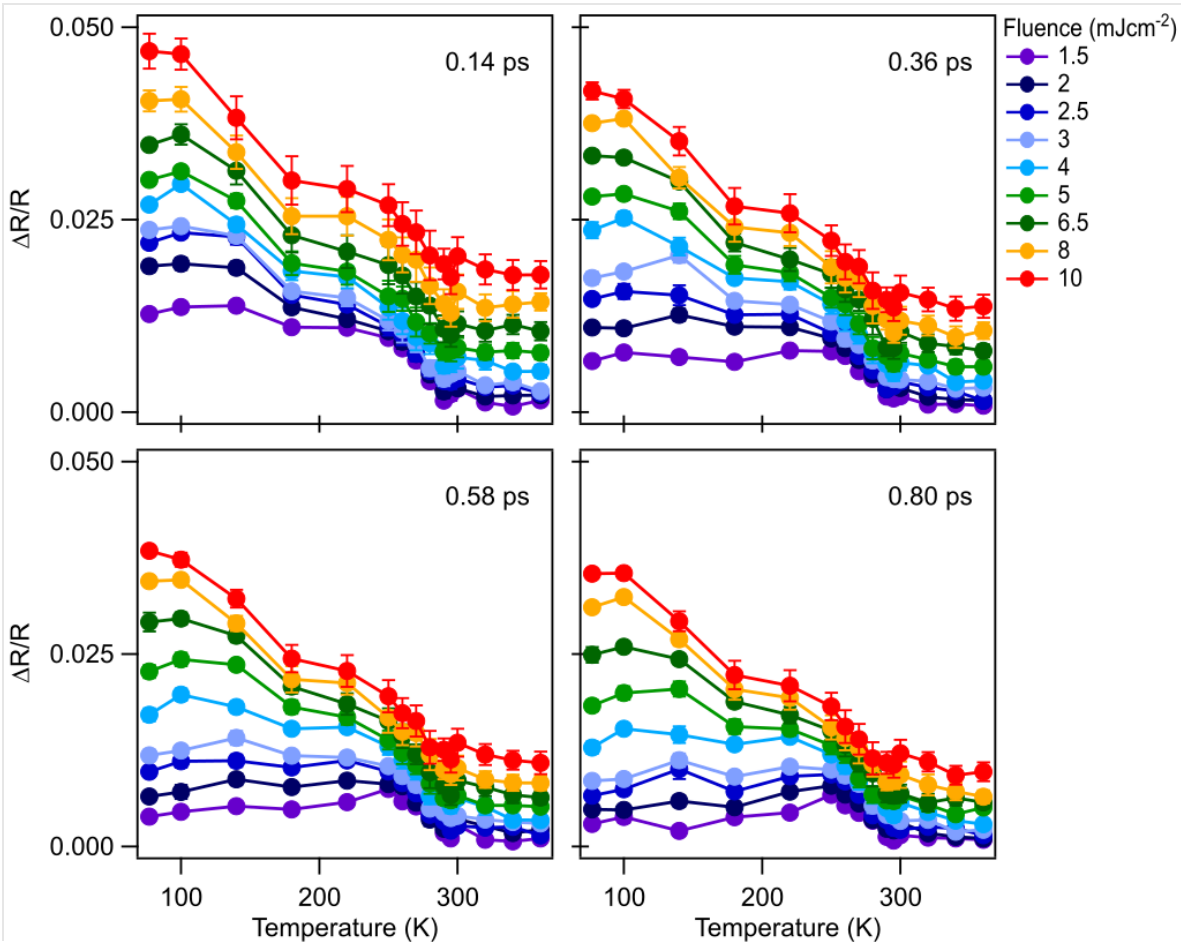

Figure S3: Temperature dependence of the transient reflectivity in the 610-622 nm range at different excitation fluences measured at a time delay of 0.14 ps, 0.36 ps, 0.58 ps and 0.80 ps. This wavelength is both sensitive to magnetic order while showing a temperature independent response above T_N. This behavior is observed at all measured fluences and time delays.

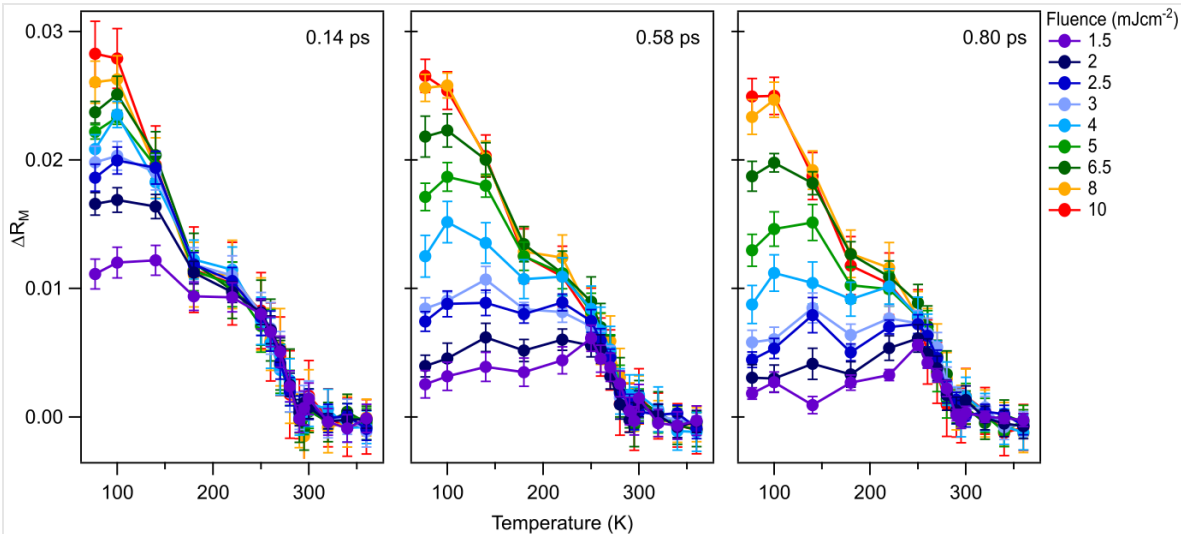

Figure S4 Temperature dependence of the magnetic degree of freedom (ΔR_M) at different excitation fluences measured at a time delay of 0.14 ps, 0.58 ps and 0.80 ps.

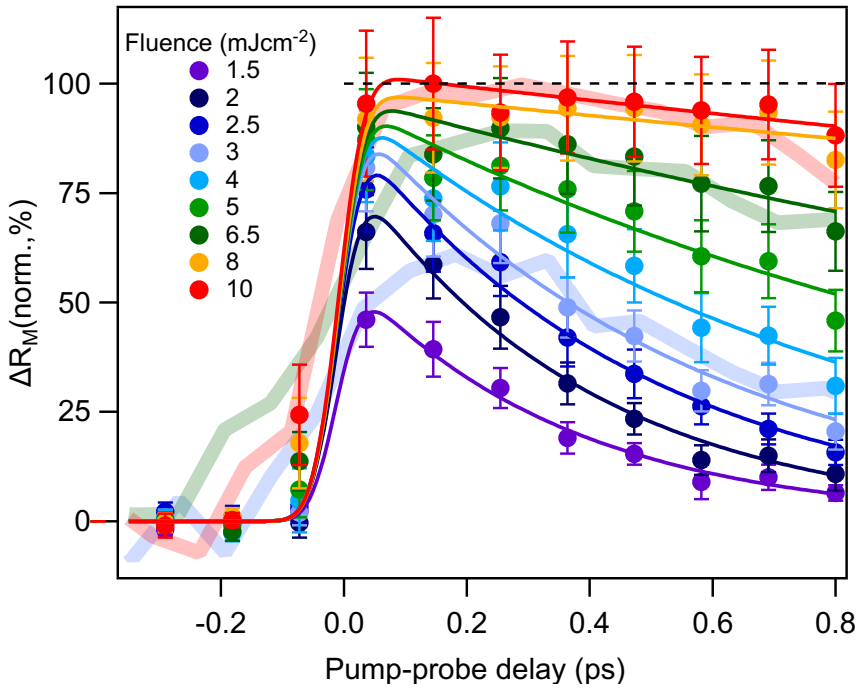

Figure S5: Time-evolution of the magnetic signal measured at 77 K at different fluence, extending the data in Figure 3D (main text). For comparison, the time evolution of the magnetic Bragg peak obtained from [4] is also shown (solid translucent lines, scaled).

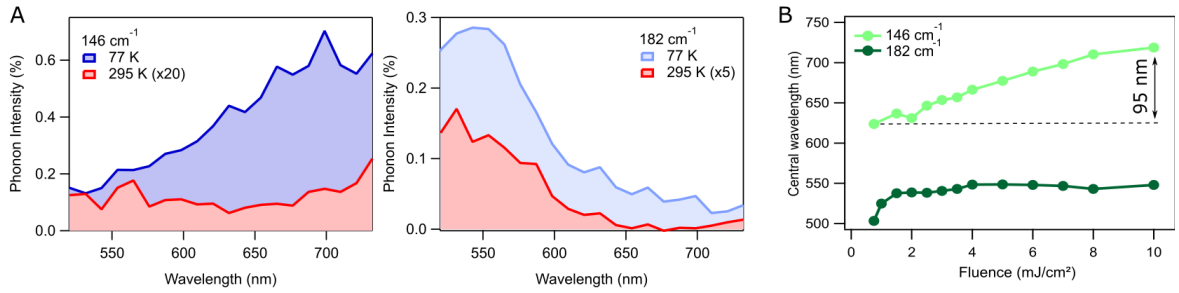

Figure S6: (A) Comparison of the spectral response of the two A_{1g} mode at 8 mJcm^{-2} as a function of temperature. The spectral dependence of the ~146 cm^{-1} mode at 77 K has a Gaussian shape centered at 700 nm while at 295 K the spectra becomes broader and featureless. In contrast, the spectral shape of the ~182 cm^{-1} mode is similar above and below Néel temperature with a reduced amplitude. For clarity, due to the amplitude differences, the spectral response intensity of both modes at 295 K has been multiplied by a constant factor. (B) Shift of the central frequency of the phonon spectra at 77 K. The ~146 cm^{-1} frequency mode shifts by ~100 nm within 1 to 10 mJcm^{-2} while the central wavelength of the ~182 cm^{-1} frequency mode shows no significant change in the same fluence region.

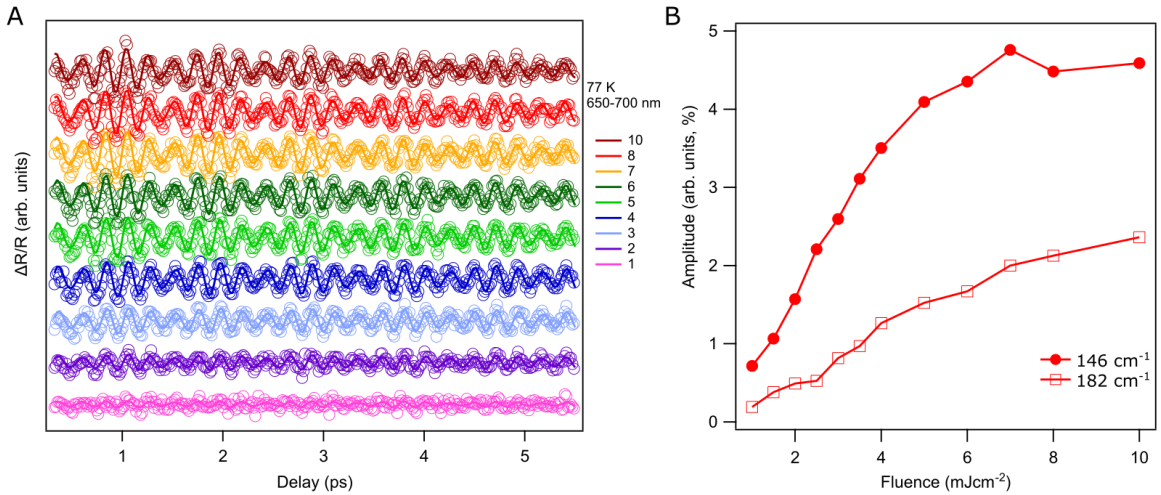

Figure S7: Fluence dependence on the phonon modes. (A) Fit of the differentiated transient data at 77 K and different fluence at 650-700 nm. The circles represent the raw data while the solid lines are the corresponding fit. (B) Amplitude parameter of ~146 cm^{-1} and ~182 cm^{-1} modes as a function of fluence obtained through the fitting procedure.

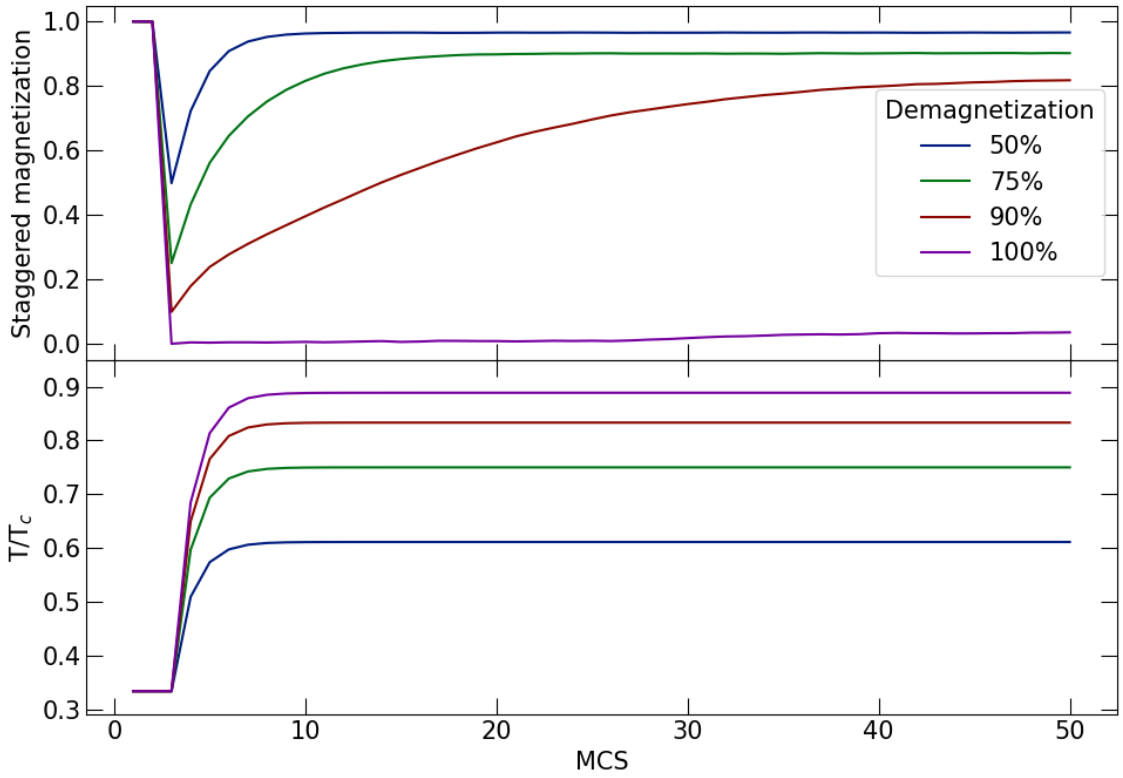

Figure S8 Magnetization dynamics (top) and temperature profile (bottom) of a Monte Carlo 3D spin-1/2 Ising model. Details on the simulation are discussed in the text.

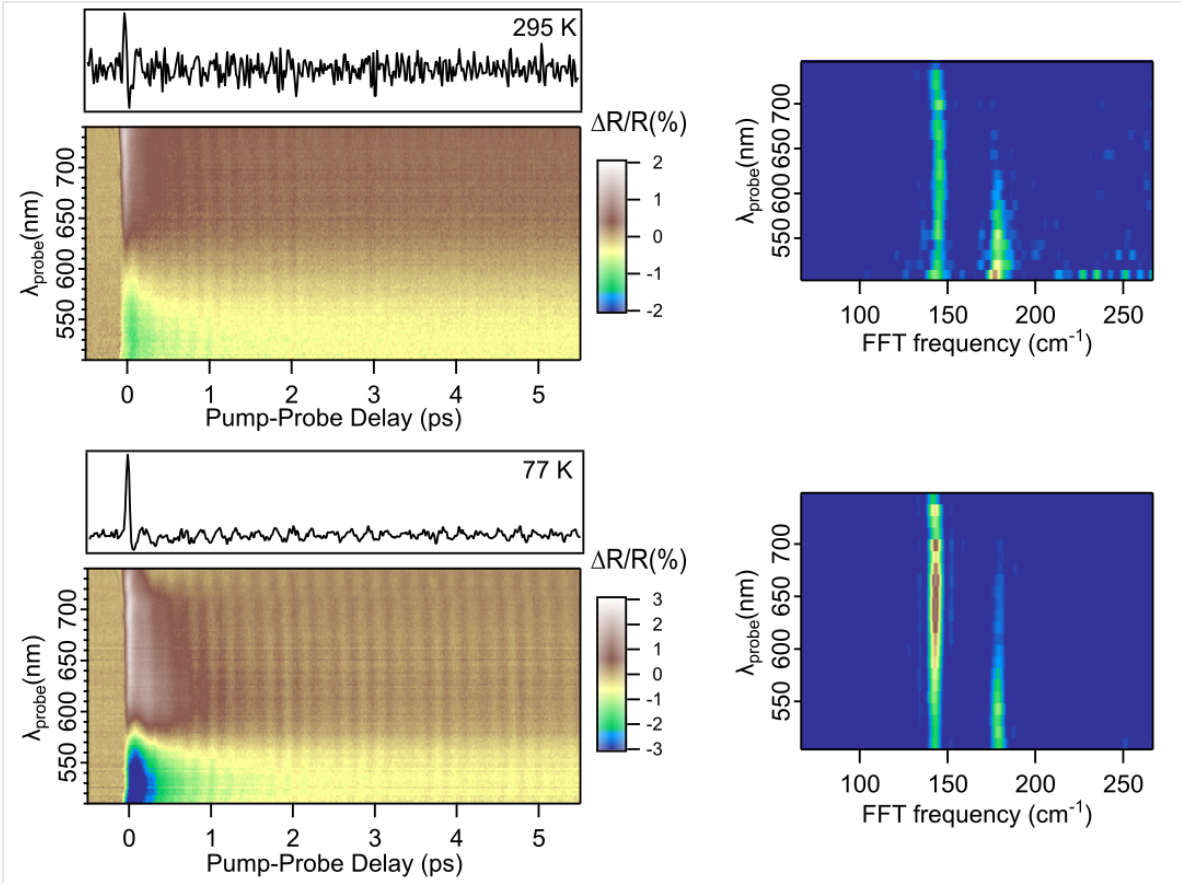

Figure S9 (A) Differentiation of the transient reflectivity change upon 800 nm excitation (F= 2.5 mJ cm^{-2}) at 295 K and 77 K. (B) Fourier transform of the oscillations in the transient reflectivity at 295 K and 77 K for each wavelength.

6. References

[1] L. Li, P. P. Kong, T. F. Qi, C. Q. Jin, S. J. Yuan, L. E. DeLong, P. Schlottmann, and G. Cao, *Tuning the Jeff=1/2 Insulating State via Electron Doping and Pressure in the Double-Layered Iridate Sr3Ir2O7*, Phys. Rev. B **87**, 235127 (2013).

[2] H. Gretarsson, N. H. Sung, M. Höppner, B. J. Kim, B. Keimer, and M. Le Tacon, *Two-Magnon Raman Scattering and Pseudospin-Lattice Interactions in Sr2IrO4 and Sr3Ir2 O7*, Phys. Rev. Lett. **116**, 17 (2016).

[3] L. L. Hu, M. Yang, Y. L. Wu, Q. Wu, H. Zhao, F. Sun, W. Wang, R. He, S. L. He, H. Zhang, R. J. Huang, L. F. Li, Y. G. Shi, and J. Zhao, *Strong Pseudospin-Lattice Coupling in Sr3Ir2O7 : Coherent Phonon Anomaly and Negative Thermal Expans*, Phys. Rev. B **99**, 094307 (2019).

[4] D. G. Mazzone, D. Meyers, Y. Cao, J. G. Vale, C. D. Dashwood, Y. Shi, A. J. A. James, N. J. Robinson, J. Lin, V. Thampy, Y. Tanaka, A. S. Johnson, H. Miao, R. Wang, T. A. Assefa, J. Kim, D. Casa, R. Mankowsky, D. Zhu, R. Alonso-Mori, S. Song, H. Yavas, T. Katayama, M. Yabashi, Y. Kubota, S. Owada, J. Liu, J. Yang, R. M. Konik, I. K. Robinson, J. P. Hill, D. F. McMorrow, M. Först, S. Wall, X. Liu, and M. P. M. Dean, *Laser-Induced Transient Magnons in Sr 3 Ir 2 O 7 throughout the Brillouin Zone*, Proc. Natl. Acad. Sci. **118**, e2103696118 (2021).

[5] H. Christiansen, S. Majumder, and W. Janke, *Phase Ordering Kinetics of the Long-Range Ising Model*, Phys. Rev. E **99**, 011301 (2019).

[6] S. Marais, V. Heine, C. Nex, and E. Salje, *Phenomena Due to Strain Coupling in Phase Transitions*, Phys. Rev. Lett. **66**, 2480 (1991).

[7] S.-H. Lee, J. S. Goh, and D. Cho, *Origin of the Insulating Phase and First-Order Metal-Insulator Transition in 1T−TaS2*, Phys. Rev. Lett. **122**, 106404 (2019).